

In situ monitoring of electrosprayed water microdroplets using laser and LED light attenuation technique: Comparison with ultra-high-speed camera imaging F


Cite as: J. Appl. Phys. **129**, 183305 (2021); <https://doi.org/10.1063/5.0046593>

Submitted: 04 February 2021 . Accepted: 21 April 2021 . Published Online: 11 May 2021

 Mário Janda,  Mostafa E. Hassan,  Viktor Martišovič,  Karol Hensel, Michal Kwiatkowski,  Piotr Terebun,  Joanna Pawłat, and  Zdenko Machala

COLLECTIONS

Note: This paper is part of the Special Topic on Plasma-Liquid Interactions.

 This paper was selected as Featured



View Online



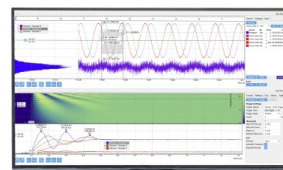
Export Citation



CrossMark

Challenge us.

What are your needs for periodic signal detection?



Zurich
Instruments

In situ monitoring of electrosprayed water microdroplets using laser and LED light attenuation technique: Comparison with ultra-high-speed camera imaging

Cite as: J. Appl. Phys. **129**, 183305 (2021); doi: [10.1063/5.0046593](https://doi.org/10.1063/5.0046593)

Submitted: 4 February 2021 · Accepted: 21 April 2021 ·

Published Online: 11 May 2021



View Online



Export Citation



CrossMark

Mário Janda,^{1,a)}  Mostafa E. Hassan,¹  Viktor Martišovič,¹  Karol Hensel,¹  Michal Kwiatkowski,²
Piotr Terebun,²  Joanna Pawłat,²  and Zdenko Machala¹ 

AFFILIATIONS

¹Division of Environmental Physics, Faculty of Mathematics, Physics and Informatics, Comenius University, Mlynska dolina, 84248 Bratislava, Slovakia

²Institute of Electrotechnics and Electrotechnology, Electrical Engineering and Computer Science Faculty, Lublin University of Technology, 38A Nadbystrzycka St., 20-618 Lublin, Poland

Note: This paper is part of the Special Topic on Plasma-Liquid Interactions.

^{a)}**Author to whom correspondence should be addressed:** mario.janda@fmph.uniba.sk

ABSTRACT

An electrostatic spray (ES) of liquids is a simple way to generate microdroplets with a high surface-to-volume ratio. The ES generated by electrical discharges enables a fast transfer of reactive species from plasma into the liquid for an efficient generation of plasma-activated water. Here, we present a relatively simple, versatile, and cost-effective diagnostic technique for online monitoring of ES microdroplets which enables simultaneous and synchronized electrical and optical diagnostics of an electrical discharge. This technique is based on planar laser light attenuation monitored by a large area photo-detector covered by a slit. Two variants were tested and compared—one with two lasers and another with one laser and a broadband LED lamp. This technique enables estimations of the speed and size of microdroplets (down to $\sim 10\mu\text{m}$) and allows for monitoring the dripping frequency or studying fragmentation of microdroplets and water filaments. The ES characteristics obtained by this technique were successfully verified by ultra-high-speed camera imaging.

Published under an exclusive license by AIP Publishing. <https://doi.org/10.1063/5.0046593>

NOMENCLATURE

A_{block}	=	Area blocked by the microdroplet
A_{eff}	=	Effective active area of the detector
A_j	=	Surface area of j th droplet
A_{mon}	=	Size of the area monitored by the detector
d	=	Droplet diameter
DC	=	Direct current
d_s	=	Small droplets limit value
ES	=	Electrospray
fps	=	Frames per second
HS	=	High speed
HV	=	High voltage
I_o	=	Optical signal intensity without microdroplets

LED	=	Light emitting diode
Q_w	=	Water flow rate
S_{horiz}	=	Width of horizontally oriented slit covering detector
S_{vert}	=	Width of vertically oriented adjustable slit
UHS	=	Ultra-high-speed
v	=	Speed of microdroplets
V_a	=	Applied voltage
v_z	=	z component of the microdroplets velocity vector

Greek

δ	=	Correction factor for intermediate droplets size calculation
ΔI	=	Optical signal attenuation
ζ	=	Zoom factor

- σ_d = Microdroplet cross section
 τ_j = Lifetime of j th droplet
 ψ = Solvation capability
 ψ_t = Solvation capability per unit time
 ψ_v = Solvation capability per unit water volume

I. INTRODUCTION

The electrostatic spray of liquids (also called electrohydrodynamic atomization), here simply called electrospray (ES), is a process to generate liquid microdroplets by a strong electric field. The application of sufficiently high voltage on the capillary (or nozzle) influences the formation of droplets from an outflowing liquid. The effective surface tension of the liquid starts to decrease due to the presence of the electric field, causing charge separation inside the liquid. For this reason, the volume of the forming droplets decreases. When a critical voltage is reached, the shape of the outflowing droplet changes to conical, referred to as a Taylor cone.¹ Finally, a jet emerges from the tip of the Taylor cone and breaks into droplets due to various instabilities.^{2,3} These charged droplets are then accelerated by the electric field and electrospray occurs. The droplets may further explode if their charge exceeds the Rayleigh limit.^{4,5}

The pioneering experimental studies describing several ES modes were conducted by Zeleny in 1914 and 1917,^{6,7} more than a century ago. Despite a long history, the research of ES is still under progress,^{8–10} and recently several reviews were published focused on different aspects of the ES.^{11–13} The key motivation of this research is a high application potential of ES in many areas including ion mobility spectrometry, powder production and surface coating, thin film deposition, gas conditioning in terms of temperature and humidity, exhaust gas treatment for an abatement of harmful gases and suspended particles, bio-decontamination, and pharmaceutical and biomedical applications.^{14–20} In most of the ES applications, the electrosprayed liquid is not pure water. The reason is the high surface tension of water. The formation of water electrospray requires such a strong electric field that leads to the generation of electrical corona discharge near the nozzle. Pulsed streamer corona discharge disrupts steady ES in a so-called cone-jet mode,^{21–23} which exists only without a discharge or with a pulseless corona discharge regime.²⁴

On the other side, the simultaneous occurrence of the discharge and the ES is beneficial for the generation of so-called plasma activated water, with potential applications in agriculture (e.g., seed germination and plant growth promotion, pest control) or in medicine (e.g., wounds healing or inactivation of cancer cells).^{25–29} The discharge generates reactive species in the gas phase and the transformation of bulk water into fine droplets results in an increase in the surface-to-volume ratio and thus accelerates the transport of reactive plasma species into the water. This concept has been adopted by several research groups^{30–33} as well as in our previous works.^{19,28,34} For instance, two different cold air plasma sources (streamer corona and transient spark discharge) were used to prepare plasma-activated water by the electrospray of fine aerosol droplets directly through the active plasma zone, which resulted in a very efficient transfer of gaseous reactive species into water. Despite many research efforts, the transport of reactive species from plasma to microdroplets is still not completely understood, because of the

complexity of this problem. Simplified studies under controlled conditions could therefore bring valuable information. For example, Oinuma *et al.* studied OH radical transfer in plasma–microdroplets interaction, using droplets’ dispenser for on-demand generation of single-size microdroplets.³¹ Monodisperse single size microdroplets can be also generated in ES with glow corona discharge,²⁴ but pulsed discharges (streamer corona or transient spark) generate polydisperse microdroplets with different diameters. It is important to study the transport mechanism of the plasma reactive species into water droplets of various sizes, but at the same time it is also crucial to monitor droplets’ size during the experiment.

The size of charged droplets can be estimated from the measured electric current.³ However, for an accurate estimate of droplets’ size, it is necessary to distinguish between discharge current and the current carried by charged microdroplets. It is possible to separate these two currents in the case of continuous glow corona discharge.²⁴ However, it can be much more complicated in pulsed discharges, especially in the case of transient spark, with current pulses significantly higher than the current pulses from microdroplets. Imaging techniques are also frequently used to monitor ES.^{35–38} Modern fast cameras enable recording videos with a high frame rate for ES visualization and enable obtaining droplets’ size from camera photographs. However, the process is quite laborious and requires post-processing of the obtained photographs. Moreover, the camera imaging technique requires a strong backlight, and this disables simultaneously detection of optical emission from the discharge.

There are several other techniques available for droplets’ diagnostic. They include imagery techniques based on shadowgraphs and holography, diffractometry, particle-sizing interferometry, and optical counters based on light scattering (see Ref. 39 and references therein). Based on these techniques, several probes were developed, useful, for example, for wet steam investigation in power plants.^{40,41} However, these probes and some of these methods are not suitable for droplets’ characterization in small gaps used to generate ES with the discharge. For ES characterization, several authors also used phase Doppler anemometry.^{22–24,42} This technique allows measuring the size distribution and velocity of droplets, as well as their concentration. The measurement point is determined by the intersection of two focused laser beams. As a particle moves through the measurement point, it scatters light from both laser beams, generating an optical interference pattern. The light collecting optics projects a fraction of the scattered light onto multiple detectors. Each detector converts the optical signal into a Doppler burst with a frequency linearly proportional to the particle velocity. The phase shift between the Doppler signals from different detectors is a direct measure of the particle diameter.

Here, we present several variants of a cost-effective optical diagnostic technique for microdroplets’ diagnostic. It was primarily developed for online monitoring of ES microdroplets during experiments where the transfer of molecules from gas to microdroplets was studied.⁴³ This technique is based on either a planar laser beam or incoherent LED light attenuation, and its use is compatible with electrical and optical discharge diagnostics. This technique enables synchronized recording of electrical signals (current from a discharge and/or microdroplets) and the optical signal (the planar laser or incoherent LED light) and the estimation of droplets’ diameter and

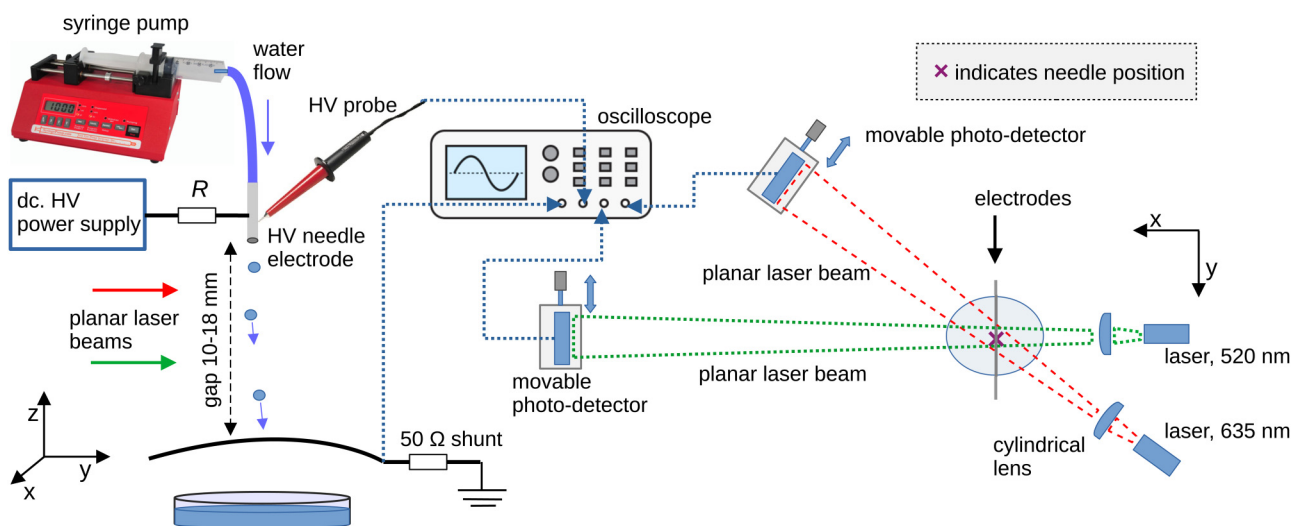


FIG. 1. Setup with two lasers, and the schematic of ES generation. Left: side view; right: top view.

speed. The results obtained by this optical diagnostic technique were confronted with results obtained by camera imaging, using two different cameras—a compact digital high-speed (HS) camera and a sophisticated ultra-high-speed (UHS) camera.

II. EXPERIMENTAL SETUP AND METHODS

The experimental setup shown in Figs. 1 and 2 consists of several sub-units, and it has several variants. Figure 1 (left part)

shows the side view of a simplified schematic diagram of the ES experimental setup. It consists of a positive DC high voltage (HV) power supply (Spellman 210-30R) and a syringe pump (New Era NE-300), which continuously supplies the de-ionized water (with conductivity $<3 \mu\text{S}/\text{cm}$) through a silicon tubing under a controlled flow rate ($Q_w = 40\text{--}1000 \mu\text{l}/\text{min}$) into a blunt hollow needle electrode (anode) nozzle with the outer and inner diameters of 0.7 and 0.5 mm, respectively. The needle electrode is placed opposite to a bent wire of 1.5 mm diameter used as a grounded electrode

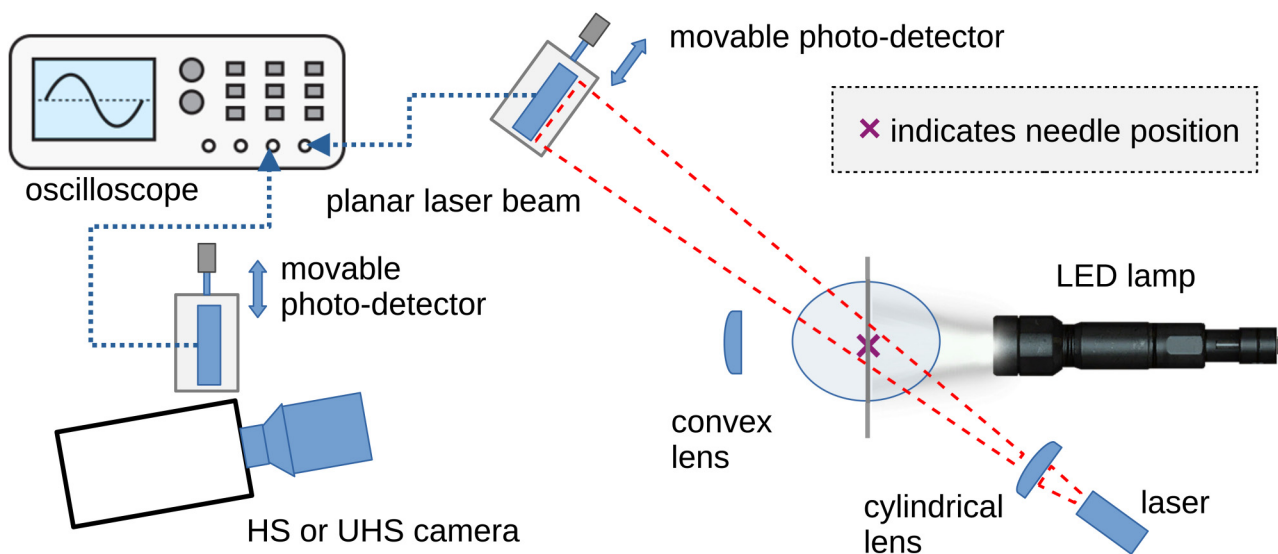


FIG. 2. Setup with one laser, LED flash lamp, and camera.

(cathode). The two electrodes are in point-to-wire geometry, both are stainless-steel with the gap size variable in a range of 10–18 mm. The HV signal from the power supply is applied through a ballast resistor of $R = 13.5 \text{ M}\Omega$ to the needle electrode. The applied voltage V_a is measured using a DC HV probe (Agilent N2771A) and then processed by a digital oscilloscope (Tektronix TBS2104). The discharge current pulses and current carried by charged microdroplets is measured on a $50 \text{ }\Omega$ resistor shunt connected to the grounded electrode.

Figure 1 (right part) shows the top view of a simplified schematic of the optical diagnostic technique for monitoring generated microdroplets using two planar laser beams. Two elliptical beams from red (635 nm) and green (520 nm) diode lasers (Thorlabs CPS635, and CPS520, 4.5 mW each) pass through cylindrical lenses, become planar, and then intersect with the droplets electrospayed from the needle electrode. The beam from the red laser is placed above the beam from the green laser, closer to the nozzle. The distance between the laser beam planes and the distance from the nozzle is varied. The lasers of different wavelengths are used for a purpose to enable selective filtering by interference filters if needed.

A variant of this technique with one laser only was also tested (Fig. 2). The lower green laser was replaced by a high power broadband flash LED lamp (Ledlenser P7R, 1000 lm). In this case, the cylindrical lens was replaced by a convex lens (focal length 200 mm, diameter 2", UV fused silica bi-convex lens, uncoated) placed between the detector and the light source.

The optical signals of the lasers and the LED lamp are detected by photodetectors (Thorlabs DET36A) and processed by a digital oscilloscope. The photodetectors are placed on micrometric translation stages. The active area of these detectors is 13 mm^2 ($3.6 \times 3.6 \text{ mm}$), but the used effective active area of detectors A_{eff} is smaller. It is given by the horizontally oriented optical slits covering the detectors, with the length of 3 mm and the slit width of $S_{horiz} = 100$ or $150 \text{ }\mu\text{m}$ (Thorlabs S100RD and S150RD), for green and red laser detectors, respectively. Additionally, A_{eff} can be modified by an adjustable slit (Thorlabs VA100/M) placed vertically in front of the detector (slit width $S_{vert} = 0\text{--}6 \text{ mm}$). We varied S_{vert} in the range of 0.5–3 mm.

The droplets passing through the planar laser beam cause signal attenuation (ΔI) related to the microdroplet cross section (σ_d) and size of the area monitored by the detector (A_{mon}) in the plane perpendicular to the laser beam in the position where it is crossed by the microdroplet. The relative attenuation of the signal can be expressed as

$$\frac{\Delta I}{I_o} \approx \frac{A_{block}}{A_{mon}}, \tag{1}$$

where A_{block} is the area blocked by the microdroplet and I_o is the optical signal intensity without microdroplets. We verified this approach by measuring a relative attenuation of the signal caused by thin wires (thickness of ~ 100 and $\sim 150 \text{ }\mu\text{m}$) introduced into the reactor through the needle electrode.

The value of A_{mon} can be calculated from the detector effective active area A_{eff} , taking into account the horizontal divergence of the planar beams. Due to divergence, A_{mon} is smaller than A_{eff} by a zoom factor $\zeta = 1.25\text{--}4.7$, determined by the relative position of the

detector and cylindrical lens. For example, for $S_{horiz} = 100 \text{ }\mu\text{m}$, $\zeta = 4.7$ and for $S_{vert} = 2.5 \text{ mm}$, $A_{mon} = 100 \times 2500 / 4.7 \text{ }\mu\text{m}^2 \approx 53 \text{ }200 \text{ }\mu\text{m}^2$. When using the LED lamp, the zoom is not only horizontal; therefore, $A_{mon} = A_{eff}/\zeta^2$, and the zoom factor ($\zeta \approx 2\text{--}4$) is determined by the relative position of the detector and the convex lens.

The area blocked by the microdroplet A_{block} depends on the microdroplet cross section σ_d . We assume spherical microdroplets: $\sigma_d = \frac{1}{4}\pi d^2$, where d is the diameter of the microdroplet. Under this assumption, we can express d as a function of ΔI . However, there is no single expression valid for all diameters. If d is smaller or equal to a certain critical value d_s , the largest covered area is equal to σ_d (Fig. 3). For lasers, $d_s = S_{horiz}$ while for the LED signal, $d_s = S_{horiz}/\zeta$. Under these conditions, we can estimate d using the following formula:

$$d = \left(\frac{4}{\pi} \left(\frac{\Delta I}{I_o} \right) A_{mon} \right)^{1/2}. \tag{2}$$

The shadow of larger droplets is never entirely projected onto the detector entrance slit. For $d > 4 \times d_s$, we can consider the blocked part of A_{mon} to be a rectangle with area $A_{block} = d_s \times d$. For "big" microdroplets, we thus get the formula

$$d \approx \frac{1}{d_s} \left(\frac{\Delta I}{I_o} \right) A_{mon}. \tag{3}$$

For droplets with $d \in (d_s, 4 \times d_s)$, we introduce a correction factor δ in order to estimate the droplet size as

$$d \approx \frac{1}{d_s} \left(\frac{\Delta I}{I_o} \right) A_{mon} + \delta. \tag{4}$$

The correction factor δ decreases linearly from a maximum value (for $d = d_s$) down to 0 for $d = 4 \times d_s$. The maximum value of δ was selected so that for $d = d_s$, the formulae (2) and (4) give the same result. In practice, we first estimated the diameter of all droplets using Eq. (2). Then, we calculated a new diameter for droplets with $d > d_s$ by Eq. (3) without the correction factor. Next, we added δ to meet the criterion mentioned above. Finally, we recalculated the

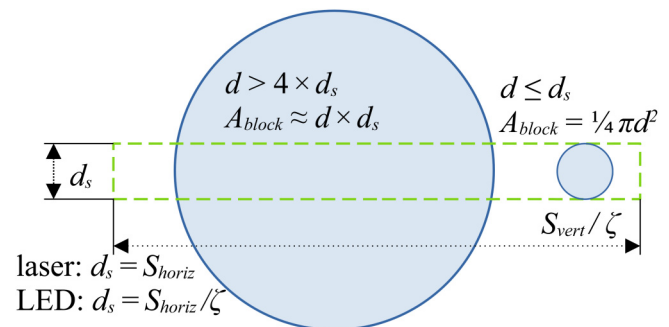


FIG. 3. Schematic comparing droplets' cross sections with area monitored by a detector.

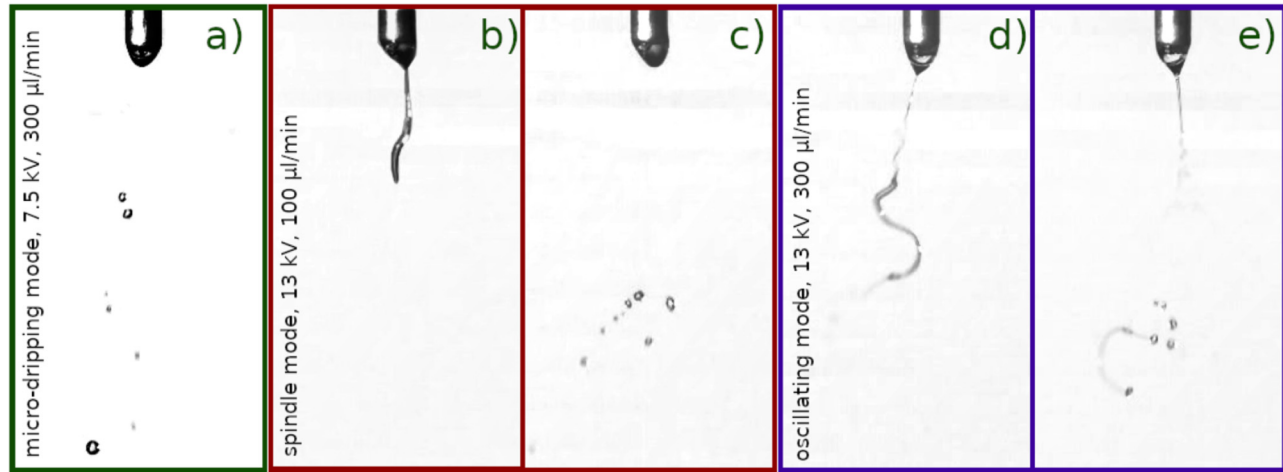


FIG. 4. Examples of water microdroplets' photographs taken by UHS camera for different V_a (kV) and Q_w ($\mu\text{l}/\text{min}$), showing different ES modes: (a) micro-dripping mode, 7.5 kV, 300 $\mu\text{l}/\text{min}$; (b) and (c) multi-spindle mode, 13 kV, 100 $\mu\text{l}/\text{min}$; (d) and (e) oscillating mode, 13 kV, 300 $\mu\text{l}/\text{min}$.

diameter of droplets with $d > d_s$ using Eq. (4) with the appropriate correction factor. Due to this approximate approach and due to the assumption of spherical shape of microdroplets, the calculated diameter is only an estimate of the effective diameter of real irregular microdroplets. Thus, this approach must be verified and validated by an independent technique.

For the validation of laser technique, two types of cameras (Fig. 2) were used to visualize the electrospayed water microdroplets and to measure their size. First, a compact digital high-speed camera (Casio Exilim EX-FH20) was used, with a typical frame rate 60 fps (frames per second) and shutter speed of $1/40\,000$ s (exposure time $25\ \mu\text{s}$). It provided photographs of size 562×623 pixels and resolution $29.2\ \mu\text{m}/\text{pixel}$. Additionally, an ultra-high-speed camera (Photron Fastcam SA-Z type 2100K-C-32GB) was used, with a typical frame rate of 25 000 fps and shutter speed of $1/133\,333$ s and $1/50\,000$ s (exposure time of $7.5\text{--}20\ \mu\text{s}$), which provided photographs of size 840×1024 pixels and resolution $21.875\ \mu\text{m}/\text{pixel}$.

To improve the contrast of the camera at short exposure times, sufficient light illumination was needed. The droplets were illuminated with two strong light sources, either white LED light (Ledlenser P7R) placed in front of the HS camera with the droplets in between or a spotlight (Dedolight Daylight 400D) placed beside the UHS camera focused to the microdroplets. The recorded HS/UHS camera photographs of the electrospayed water microdroplets were processed and analyzed by the software Microsoft Office Picture Manager and GNU Image Manipulation Program.

III. RESULTS AND DISCUSSION

This section is divided into three subsections. In the first subsection, results obtained by UHS camera imaging of water electro-spray are presented. This technique is well established, and it is used as a benchmarking tool. In the second subsection, the results

obtained by the laser technique are presented and capabilities of this technique are discussed. The third subsection is dedicated to the comparison of the used UHS camera imaging and laser-based techniques.

A. UHS camera microdroplet imaging

When the applied voltage (V_a) on the needle nozzle through which water is delivered with a water flow rate (Q_w) is progressively increased, the size of generated droplets gradually decreases. The ES onset voltage depends on the gap size and the water flow rate. With the gap is 10 mm, the ES initiates at ~ 4.5 kV, while when the gap size is 15.8 mm, the ES initiated at 7.5 kV (at the lower Q_w). Figure 4 shows an example of photographs of electrospayed microdroplets obtained by UHS camera, with the gap of 15.8 mm. We observed several ES modes depending on the applied voltage and the water flow rate (Table I): micro-dripping mode [Fig. 4(a)], spindle mode, multi-spindle mode [Figs. 4(b) and 4(c)], and oscillating mode [Figs. 4(d) and 4(e)]. The biggest advantage of using UHS camera for ES diagnostics in comparison with other techniques presented in this paper is the possibility of recording video with a high frame rate that allows easy and unambiguous identification of the ES mode.

TABLE I. Classification of the observed ES modes, depending on applied voltage and water flow rate, gap of 15.8 mm.

ES mode	V_a (kV)	Q_w ($\mu\text{l}/\text{min}$)
Micro-dripping	7.5	100–500
Spindle	9–11	100–500
Multi-spindle	13	100
Oscillating	13	300–500

In order to simultaneously observe the formation of the Taylor cone, water filament or spindle near the nozzle [Figs. 4(b) and 4(d)], and their fragmentation in the lower part of the gap [Figs. 4(c) and 4(e)], monitoring of a large area with dimensions approximately 18.4×22.4 mm was needed. Since the UHS camera provided photographs of size 840×1024 pixels, our spatial resolution was limited to as much as $21.875 \mu\text{m}/\text{pixel}$. Despite this fact, we were able to estimate the size distribution of the water microdroplets with diameters above $\sim 20 \mu\text{m}$ from a large set of UHS camera photographs (Fig. 5). Besides V_a [Fig. 5(a)], the water flow rate Q_w also influences this size distribution. However, the differences due to varying Q_w do not seem to be very significant. In all size distribution histograms, the largest amount of microdroplets have a diameter of $d \approx 50 \mu\text{m}$, and there is only a few droplets with diameter $d > 150 \mu\text{m}$. The abundance of these “big” droplets slightly decreases with increasing V_a and decreasing Q_w .

The microdroplet size histograms were also constructed from the sets of photographs obtained by the compact HS camera and compared with UHS camera [Fig. 5(b)]. In this case, the spatial resolution was slightly lower, approximately $29.2 \mu\text{m}/\text{pixel}$. Moreover, due to longer exposure time (min. $25 \mu\text{s}$) and relatively high speed of droplets, the trail of droplets (shadow) appeared prolonged on the photographs. Furthermore, it was assumed that the droplets are spherical, and the smallest width of the observed oval shadows was taken as a diameter of spherical droplets.

The comparison of the UHS camera histograms with the histograms obtained by the compact HS camera shows that there are significant differences, with an apparently higher abundance of microdroplets with $d = 120\text{--}150 \mu\text{m}$ in the HS camera histograms. We suggest two possible explanations. First, the spatial resolution of HS camera was lower ($\sim 29 \mu\text{m}/\text{pixel}$) than UHS camera. It is possible that only some of microdroplets with $d < 60 \mu\text{m}$ were

detected. With underestimated abundance of small microdroplets in the distribution, the abundance of bigger microdroplets is probably overestimated. Next, the observed differences could be explained by a different depth of field. A smaller depth of field of the HS camera allowed us to see higher fraction of bigger and heavier droplets, which do not deviate from the focusing plane defined by electrodes.

B. Laser technique microdroplet size measurements

1. Variant with one laser

As mentioned earlier, the size of droplets gradually decreases with the increasing applied voltage. Figure 6(a) shows how the decrease in the droplet size changes the optical signal from a single planar laser beam positioned in the middle of the interelectrode gap (10 mm gap, laser beam 5 mm below the needle electrode). Big droplets block the laser signal completely. Starting from a certain size, approximately 1 mm, blocking becomes only partial, and the signal attenuation becomes smaller and smaller. The droplets' size [Fig. 6(b), left vertical axis] was estimated from the maximum signal attenuation [Eq. (3)], while the speed of droplets was estimated from the duration of the signal attenuation. The speed of droplets increases with the decreasing diameter [Fig. 6(b), right axis].

The transition from big droplets into the ES micro-dripping causes a significant change of the detected optical signal. Instead of one strong signal attenuation, a series of shorter signal attenuations is observed [Fig. 7(a)]. These signal attenuations represent microdroplets and they occur in packages [Fig. 7(b)] caused by a periodic formation of the Taylor cone on the nozzle. With the gap of 10 mm, the ES starts at $V_a \approx 4.4\text{--}4.6$ kV. This corresponds to the corona discharge onset voltage.

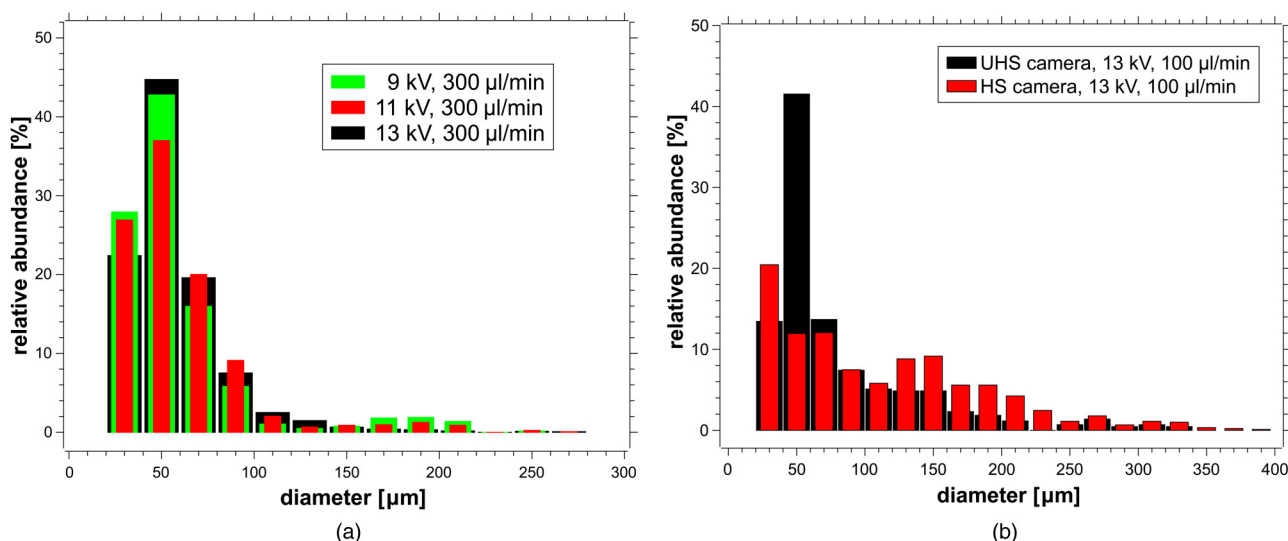


FIG. 5. The relative abundance of water microdroplets produced by ES as a function of microdroplets' diameter; (a) dependence on applied voltage V_a , $Q_w = 300 \mu\text{l}/\text{min}$, measured by UHS camera; (b) comparison of UHS and HS camera size distributions, $Q_w = 100 \mu\text{l}/\text{min}$, $V_a = 13$ kV.

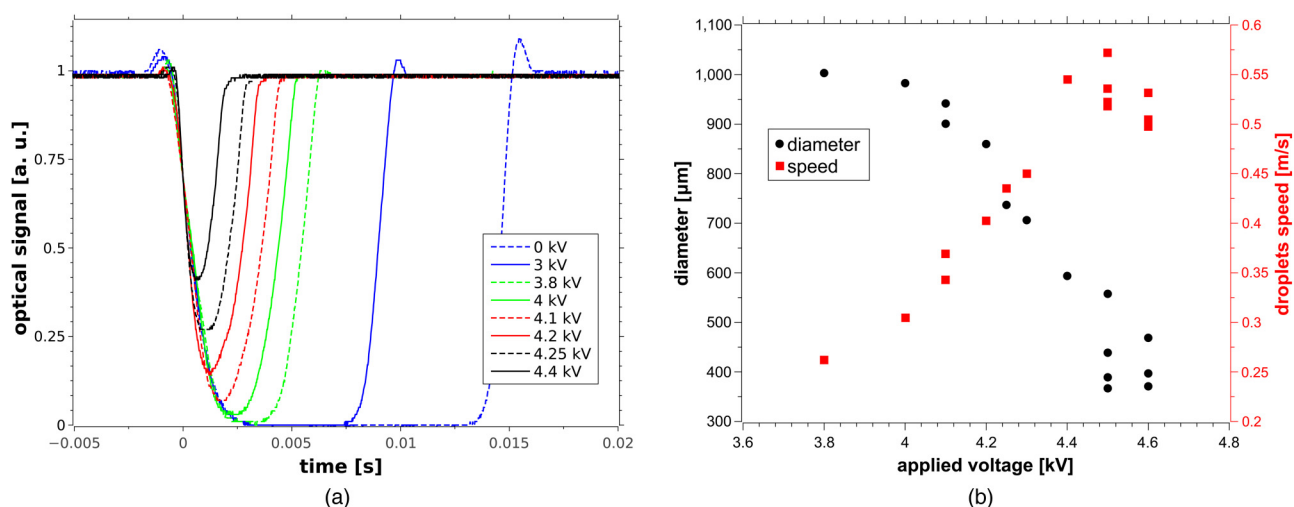


FIG. 6. Big droplets monitored by a single planar laser, dependence on V_a , $Q_w = 40 \mu\text{l}/\text{min}$, gap 10 mm, laser beam 5 mm below the nozzle; (a) optical signal changes caused by droplets; (b) estimated speed (right axis) and diameter (left axis) of droplets.

Figure 7 demonstrates one of the advantages of the presented laser technique. It enables simultaneous monitoring of microdroplets by optical and their corresponding electrical signals (currents). These two signals are processed by the same oscilloscope, and they can be easily synchronized, for example, by the optical signal attenuation caused by microdroplets, as shown in Fig. 7(a). On the other hand, it is not trivial to correlate these two signals, even if we assume that each measured current peak corresponds to a unique microdroplet flying between the electrodes. The optical signal shows only a subset of all microdroplets, i.e., those crossing the planar beam in the area

monitored by the detector. We usually maximized the number of monitored microdroplets by changing the horizontal position of the detector perpendicularly to the laser beam. However, it was not possible to detect all generated microdroplets.

More efforts are needed to study correlation between measured optical and electrical signals. We consider possibility of implementing advanced nonlinear time series analysis techniques, such as recurrence quantification analysis technique,⁴⁴ multifractal analysis, or detrended fluctuation analysis for the characterization of optical and electrical signals obtained by the technique presented

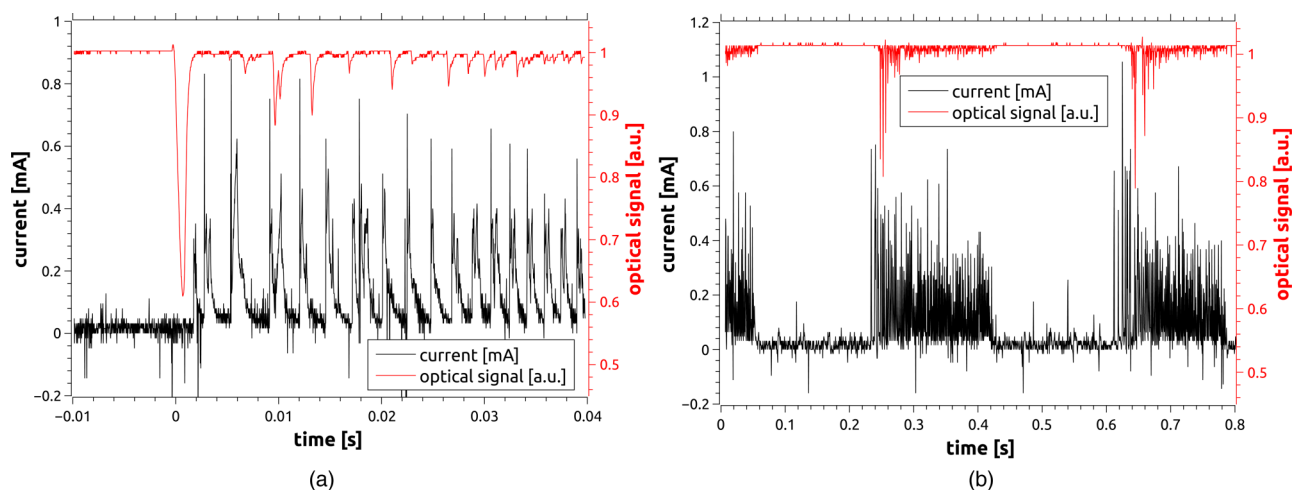


FIG. 7. Optical signal from a single planar laser and the corresponding electrical signal (current), micro-dripping ES mode, gap 10 mm, laser 5 mm below the nozzle: (a) 4.4 kV, shorter time scale; (b) 5.5 kV, longer time scale showing packages.

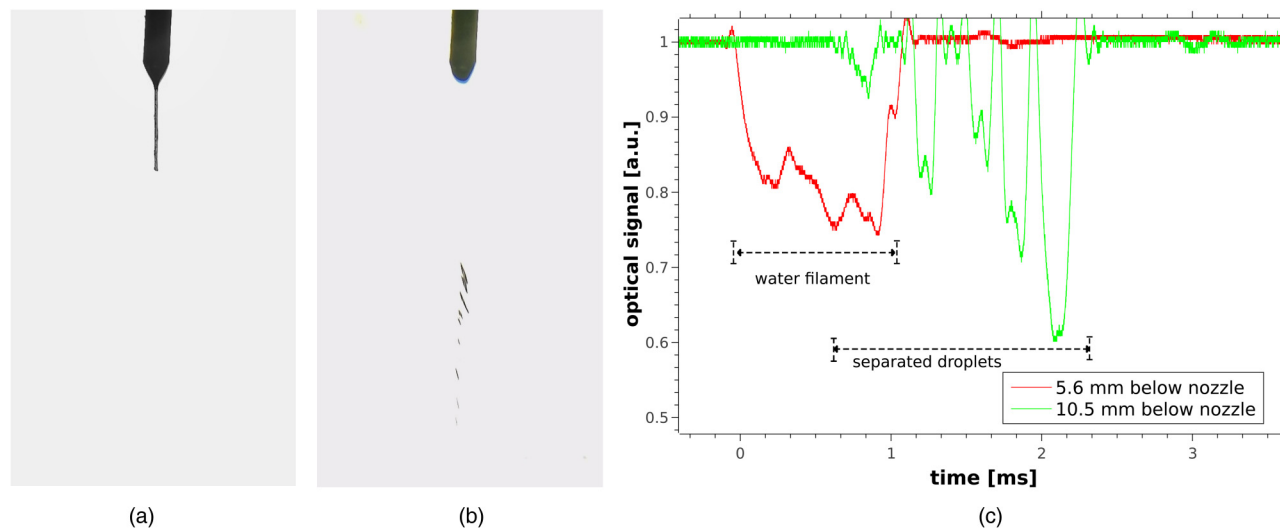


FIG. 8. Fragmentation of water filament: (a) HS camera photographs of water filament; (b) HS camera image of separated microdroplets; (c) typical optical signals corresponding to filament fragmentation; $V_a = 13$ kV, $Q_w = 100$ $\mu\text{l}/\text{min}$, gap 15.8 mm.

in this paper. The advanced time series analysis could help us to understand the nonlinear dynamical behavior of a non-steady-state ES interacting with pulsed discharges.

2. Variant with two lasers

More advantages of the presented laser technique can be demonstrated when two planar laser beams are used. There are two possible configurations when using two planar lasers. They differ by the distance of the upper laser beam from the nozzle. In the first configuration, the upper laser beam is close to the nozzle, where there are no microdroplets, but the Taylor cone (micro-dripping ES mode), or the water filament (spindle, multi-spindle, or oscillating ES modes). In this configuration, the signal of the upper laser can be used as a synchronization signal for triggering external devices, such as an optical emission spectrometer. In this work, we always synchronized oscilloscopic waveforms by upper laser optical signal attenuation.

With the upper laser close to the nozzle, the presented laser technique can be used to study the water filament fragmentation. Figures 8(a) and 8(b) show the water filament fragmentation as recorded by the HS camera (the brightness and contrast of photographs were adjusted to improve the visibility of the studied phenomenon). Figure 8(a) shows the water filament still attached to the nozzle. Figure 8(b) shows the water filament already fragmented into separated microdroplets (they look prolonged due to a relatively long exposure time of the HS camera). These photographs can be used for the interpretation of optical signals recorded by the oscilloscope [Fig. 8(c)]. The duration of the upper laser signal intensity attenuation is relatively long [Fig. 8(c), red line]. It could be used to estimate the water filament formation time. From the amplitude of signal attenuation, the diameter of the filament can be estimated. The lower green laser beam intensity shows several

shorter signal attenuations corresponding to individual microdroplets [Fig. 8(c), green line].

Next, the optical signal from the upper laser can be used to measure the frequency of the Taylor cone or water filament formation processes. Figure 9 shows the frequency of the Taylor cone or water filament formation as a function of the applied voltage for different water flow rates. The frequency decreases with the increasing applied voltage, and it is related to the changes of the ES mode. The highest frequency is in the micro-dripping mode, where it

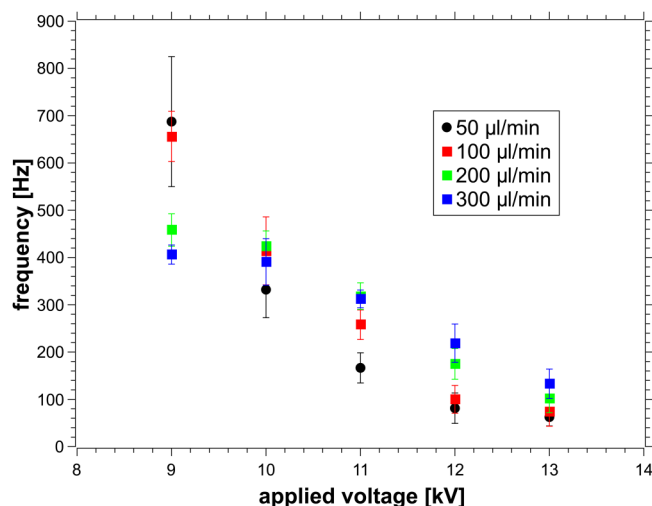


FIG. 9. Frequency of the Taylor cone or water filament formation as a function of V_a , different Q_w .

corresponds to dripping of individual droplets. With increasing voltage, the tip of the Taylor cone prolongs and the water filament is formed. This water filament separates from the nozzle less frequently than individual droplets in the micro-dripping ES mode. On the other hand, Fig. 9 shows that the transition between ES modes is not so abrupt since we observed no sudden change in the measured frequency.

If the upper laser is not too close to the nozzle, it can also be used for the detection of individual microdroplets (especially in micro-dripping ES mode). From the set of oscilloscopic records, it is also possible to construct a histogram showing droplets' size distribution. If two histograms from two different positions in the gap are available, it is possible to use this technique to study the fragmentation of microdroplets statistically as they fly through the gap. Figure 10 shows an example of the microdroplets' fragmentation measured by two lasers separated by 4.9 mm. The upper laser was 5.6 mm below the nozzle. The gap size was 15.8 mm, the applied voltage was 9 kV, and the water flow rate was 100 $\mu\text{l}/\text{min}$. The two histograms are significantly different. The size of the largest microdroplets detected 5.6 mm below the nozzle was around 270 μm , while the largest microdroplets detected 10.5 mm below the nozzle had only approximately 170 μm . The most abundant size of microdroplets decreases from approximately 70 μm (5.6 mm below the nozzle) down to around 30 μm (10.5 mm below the nozzle). However, both numbers are in relatively good agreement with most probable size of microdroplets ($\sim 50\text{--}60\ \mu\text{m}$) detected by phase Doppler anemometry in unsteady ES.²⁴ This proves that the assumption of spherical droplets used to calculate the diameter of microdroplets (see Sec. II) is sufficiently accurate, even though the real shape of microdroplets is irregular (Fig. 4). Due to irregular deformations in all directions, the observed cross section used to calculate diameter can be both, slightly smaller, or slightly larger

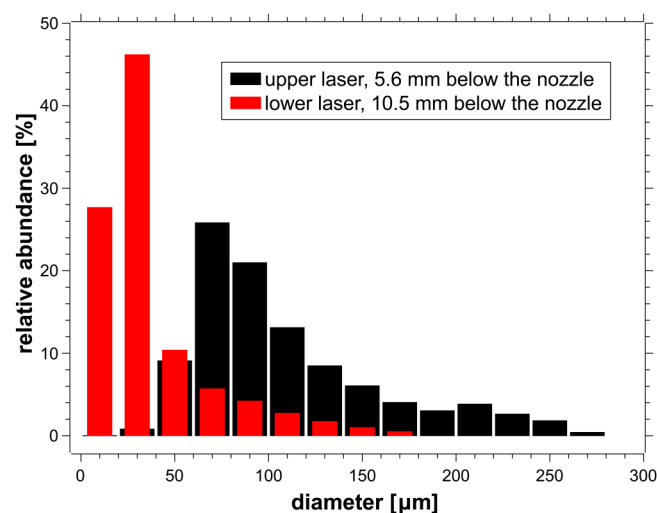


FIG. 10. Histograms showing droplets' size distribution, measured by two planar lasers at different distances from the nozzle, $V_a = 9\ \text{kV}$, $Q_w = 100\ \mu\text{l}/\text{min}$ (micro-dripping ES mode).

than the cross section corresponding to an ideal spherical microdroplet of the given volume. Therefore, the assumption of spherical microdroplets should have no significant influence on the droplets' size distribution (Fig. 10) constructed from a very large set of microdroplets.

Another possibility how to use the two-laser variant with the upper laser being not too close to the nozzle is demonstrated in Fig. 11. It can be used to estimate the speed of microdroplets from the delay between the optical signal attenuation of two lasers. Here, we must emphasize that the two lasers must be relatively close to each other (max $\sim 3\ \text{mm}$) so that the signal attenuations caused by the same microdroplet can be detected by both photodetectors. If the lasers are not close enough, it is difficult to identify and match the identical microdroplets from the two laser signals—many microdroplets do not cause attenuation in both optical signals due to the wide angle between the trajectories of different droplets and due to their fragmentation.

Figure 11 shows a comparison of speed calculated from the delay between signal attenuation of two lasers with the speed calculated from the sequence of UHS camera photographs. There is a certain difference between these two series of data points: the values obtained by the laser technique are generally lower, especially for larger droplets. Here, one should realize that the upper laser was 5.6 mm from the nozzle and the lower one only 3 mm lower, with the total gap size of 15.8 mm. Thus, the droplet speed was measured with two lasers in the upper part of the gap, while the speed from the camera photographs represents an average speed in the entire gap. Since the charged droplets accelerate as they fly across the gap, their speed in the upper part is lower than the average value. We checked this by calculating the speed of several microdroplets with a diameter of 110–175 μm at the position 5.6–8 mm below the nozzle. Here, the speed of these

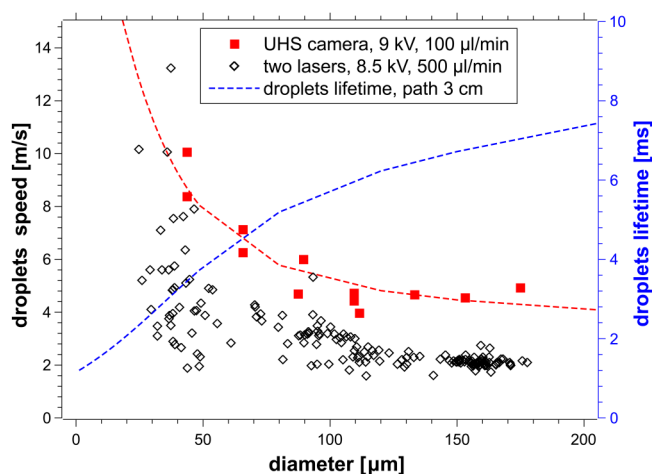


FIG. 11. Estimated speed of microdroplets from the delay between the signal attenuations of two lasers, upper laser 5.6 mm below the nozzle, lower laser 8.6 mm below the nozzle. Comparison with the microdroplets' speed calculated from a sequence of UHS camera photographs. Shown together with droplet lifetime as a function of droplet diameter, $V_a = 9\ \text{kV}$, $Q_w = 100\ \mu\text{l}/\text{min}$.

microdroplets was only around 3.3–3.7 m/s, which is comparable to the value measured by the laser technique.

In addition, it is necessary to point out here that the laser technique measures only the z component of the velocity vector v_z , while the speed derived from the camera photographs is determined by z and y components of the velocity vector. The value obtained from camera photographs is actually close to the scalar speed of the microdroplets. The depth of the field of camera is quite small, and it is possible to follow individual droplets on a sequence of photographs only if x component of the microdroplets' velocity vector is close to 0. For this reason, the speed derived from the camera photographs must be higher or equal to v_z obtained by the laser technique. In any case, the obtained values of v_z are in the same range as values reported by Ehouarn *et al.*⁴⁵

Figure 11 also shows the estimated lifetime of flying microdroplets derived from the UHS camera photographs, calculated from the fitted speed,

$$v = 2 + 20 \times \exp(-d/24) + 4 \times \exp(-d/300). \quad (5)$$

It was further assumed that the typical trajectory of a microdroplet in the reactor is 3 cm long. The lifetime of microdroplets is important from a practical point of view. ES in combination with electrical discharges can be efficiently used for the generation of plasma-activated water, as employed in our previous studies,^{19,28,34} as well as by other authors.^{32,33} The amount of species transferred from plasma into microdroplets depends on the gas phase concentration of these species, the surface area of the plasma/water interface, and the contact time of the microdroplets with the plasma.⁴³ Assuming that the contact time is identical to the lifetime of microdroplets, then the contact time is limited to a few milliseconds (Fig. 11).

3. Combination of one planar laser beam with LED lamp

In this variant (Fig. 2), the upper laser is used, but the lower laser is replaced by an incoherent light source—a high intensity LED lamp. The possible utilization of the upper laser is the same as discussed in Secs. III B 1 and III B 2 (synchronization signal, dripping frequency monitoring, or microdroplets' size distribution). The optical signal from the LED lamp is used only for microdroplets' monitoring to collect data for constructing microdroplets' size distribution histogram. This variant with the LED lamp was tested to simplify microdroplets' identification and to improve the accuracy of the microdroplets' size estimates. Using lasers, the diffraction of light on the microdroplets must be considered. The diffraction on the microdroplets crossing the beam caused secondary minima in the measured signal attenuations (Fig. 12, upper red curve, the secondary minima are labeled by a cross sign).

When a signal attenuation from well-separated microdroplets is recorded (if they crossed the beam with a sufficient delay, at least 0.5 ms), it is possible to distinguish primary and secondary (diffraction) minima in the signal attenuation caused by individual microdroplets. If the microdroplets cross the beam shortly one after another, it is difficult to separate the signal attenuations caused by the individual microdroplets. In such case, it was not possible to use these signal attenuations for the estimation of the microdroplets' size.

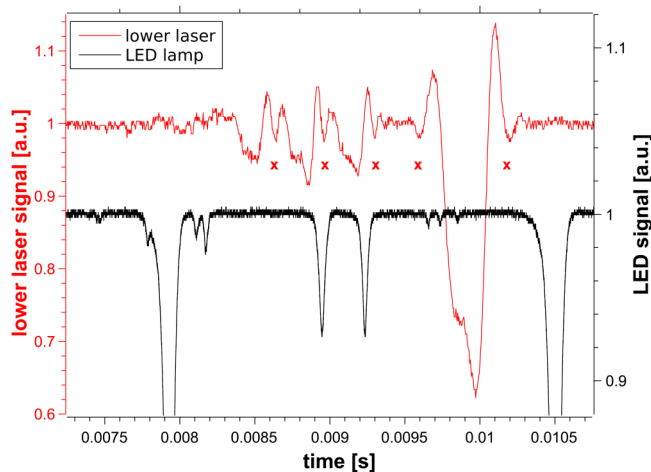


FIG. 12. Comparison of optical signals showing the signal attenuation caused by microdroplets when measured by laser (red line) and by LED lamp (black line). The crosses indicate secondary signal attenuations due to diffraction of the laser light.

When using incoherent LED light, the obtained optical signal was simpler, since no diffraction patterns were observed (Fig. 12, lower black curve). Even if the signal attenuations caused by more droplets overlapped, it was possible to fit and separate signal attenuations caused by individual microdroplets and estimate their size. Simpler LED signal enables easier post-processing of the recorded oscilloscopic waveforms, using script written in scientific programming language GNU Octave with function “findpeaks” for automatic droplet detection.

The LED lamp had a better stability of short-time light intensity than lasers and its monitored area was smaller thanks to the vertical zoom. Thus, a slightly higher sensitivity was achieved than with two lasers. The smallest relative signal attenuation that could be positively recognized as caused by a microdroplet was as low as approximately 0.5%. The estimated diameter of the smallest microdroplets is $\sim 5 \mu\text{m}$. This represents the theoretical limit of our technique, because for smaller droplets we would have to take into account geometrical as well as Mie scattering.

The disadvantage of using a strong broadband LED lamp is that simultaneous optical diagnostic of the discharge is not possible due to too strong broadband light intensity. On the other hand, when using two planar lasers, a simultaneous optical diagnostic of the ES and of the discharge (emission spectroscopy, or imaging) is possible since the laser light could be filtered by appropriate notch filters.

C. Comparison of results obtained by different techniques

1. Comparison of microdroplets size histograms

In Sec. III A, it was shown that it is possible to estimate the size distribution of the ES water microdroplets from a large set of

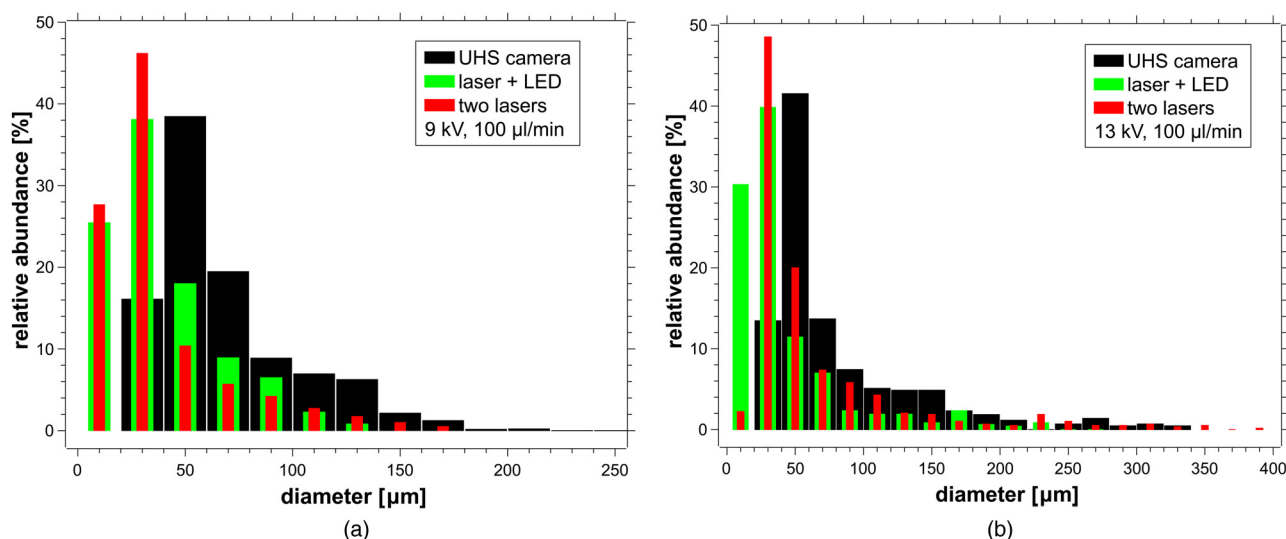


FIG. 13. Histograms showing droplets' size distribution. Comparison of three techniques, water flow rate of $100 \mu\text{l}/\text{min}$; (a) applied voltage of 9 kV; (b) applied voltage of 13 kV.

UHS camera photographs. This method is very straightforward, and we will consider the histograms constructed from UHS camera photographs as the reference histograms (Fig. 5), even though microdroplets with size $\sim 20 \mu\text{m}$ and less are below the resolution limit of this method (one pixel represents $21.875 \mu\text{m}$).

The differences between UHS camera histograms measured at different applied voltages and water flow rates do not seem to be very substantial (Fig. 5). By contrast, the differences between histograms constructed by different optical techniques are much more significant (Fig. 13). According to the laser techniques (one laser + LED lamp or two lasers), there are much more microdroplets with $d < 40 \mu\text{m}$ than detected by UHS camera.

We suppose that it is influenced by the different sensitivities of the used techniques to small microdroplets. When using one planar laser and LED light, the smallest detected microdroplets have an estimated diameter of $d \sim 5 \mu\text{m}$, although probably only some of them are detected. With two lasers, the detection limit was $\sim 10 \mu\text{m}$. The UHS camera cannot detect microdroplets of $d < 20 \mu\text{m}$ and even microdroplets with $d = 20\text{--}40 \mu\text{m}$ are probably detected with low efficiency. For this reason, we assume that only microdroplets with $d > 40 \mu\text{m}$ should be considered when comparing these different techniques. When only these microdroplets are considered, the histograms obtained by the UHS camera and laser techniques are very similar (Fig. 14).

These results impose questions on the reliability and usability of these microdroplet visualization methods if they cannot detect the smallest and the most abundant microdroplets. However, as shown in our precedent paper, the biggest microdroplets are the key factors determining achieved concentration of species solvated to microdroplets from the gas phase.⁴³ For example, if 10 ozone-saturated tiny microdroplets with $d = 10 \mu\text{m}$ are merged with 1

larger unsaturated droplet with $d = 200 \mu\text{m}$ and a saturation degree 0.1, the resulting ozone saturation degree would be only 0.100125.

2. Comparison based on the microdroplets' surface area and lifetime

It is difficult to assess differences behind relatively similar droplets size distribution histograms. For this reason, a more accurate quantitative parameter should be used for the comparison of the tested optical techniques. As mentioned earlier, the surface area and lifetime of microdroplets are important parameters determining their solvation potential of various (plasma) reactive species. For this reason, we suggest using the parameter solvation capability $\psi = \sum A_j \times \tau_j$, i.e., the sum of the product surface area A_j of the j th droplet and its lifetime τ_j .

For an accurate estimate of the solvation capability ψ , a large set of detected microdroplets is needed. Next, to be able to compare the solvation capability of ES microdroplets generated at different experimental conditions (Q_w , V_a , gap size, ...), ψ should be normalized. There are two normalization possibilities to be considered—normalization per unit time (ψ_t), and normalization per unit volume (ψ_v).

The solvation capability normalized per unit time ψ_t is influenced by the water flow rate [Fig. 15(a)]. Naturally, more molecules from the gas phase can be transferred into water if a larger amount of water is sprayed into the reactor per unit time. Thus, a coarser water aerosol can be characterized by higher ψ_t than a finer water aerosol created by ES with lower Q_w . In Fig. 15(a), we can see that ψ_t increases significantly with increasing Q_w . The increase in ψ_t with increasing applied voltage is also present, and this could be attributed to the generation of a finer water aerosol at higher

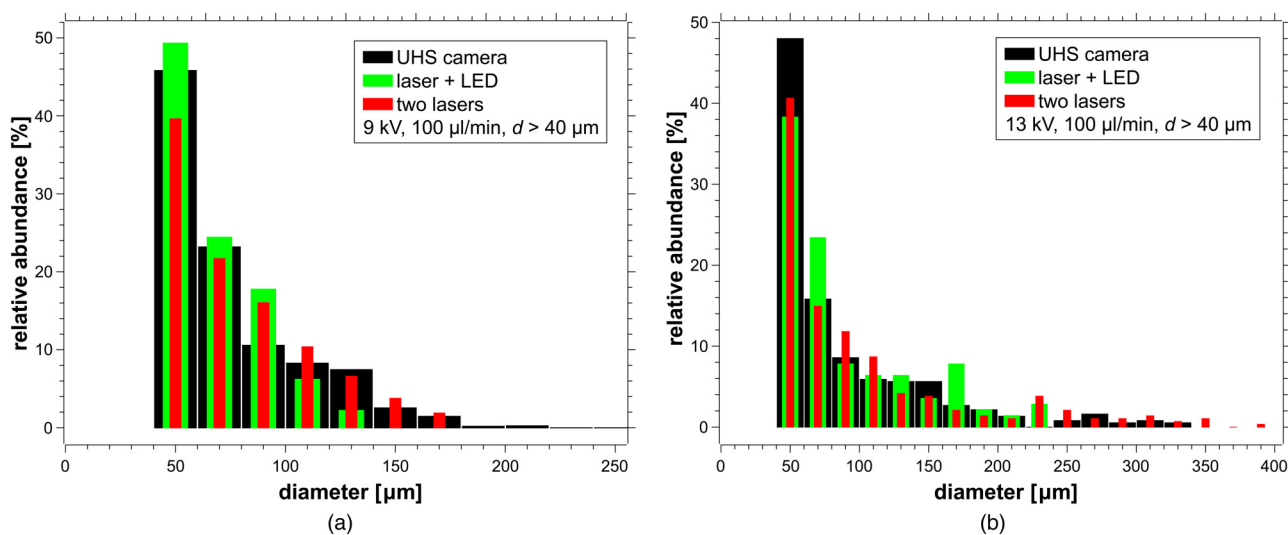


FIG. 14. Partial histograms showing droplets' size distribution, with microdroplets with $d > 40 \mu\text{m}$. Comparison of three techniques, $Q_w = 100 \mu\text{l/min}$; (a) $V_a = 9 \text{ kV}$; (b) $V_a = 13 \text{ kV}$.

voltages. The maximization of ψ_t is interesting in practice if the goal is to solvate as many reactive molecules as possible from the gas phase into the water per given treatment time, e.g., in ozonation processes.

The solvation capability per unit volume ψ_v [Fig. 15(b)] does not reflect the influence of Q_w . This parameter is more directly related to the size distribution of the ES water droplets. The higher ψ_v means that a higher concentration of solvated reactive molecules

should be achieved in the liquid phase (in the case of insignificant depletion of the gas phase concentration of solvating molecules). It is important, e.g., in producing highly active plasma activated water for biomedical applications.

Figure 15(b) shows that the highest ψ_v is achieved for the lowest water flow rate and the increase in ψ_v with increasing V_a is also obvious. There is one exception, for $Q_w = 100 \mu\text{l/min}$ and $V_a = 13 \text{ kV}$. In this case, the ES is already occasionally disrupted by

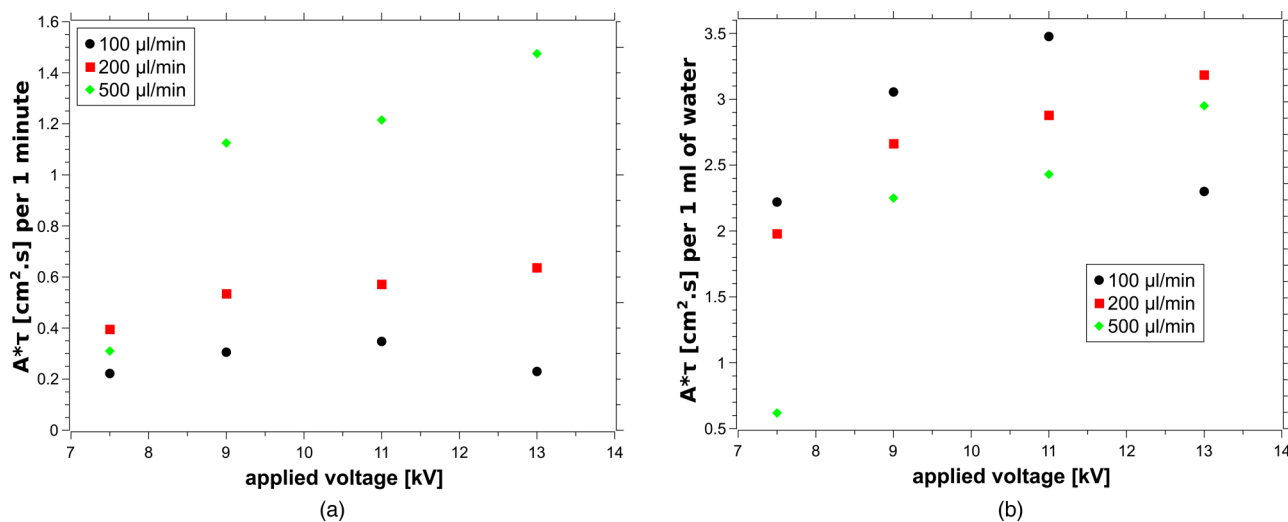


FIG. 15. The solvation capability as a function of the applied voltage, different water flow rates, gap 15.8 mm, calculated for droplets recorded by UHS camera; (a) normalized per unit time ψ_t , (b) normalized per unit volume ψ_v .

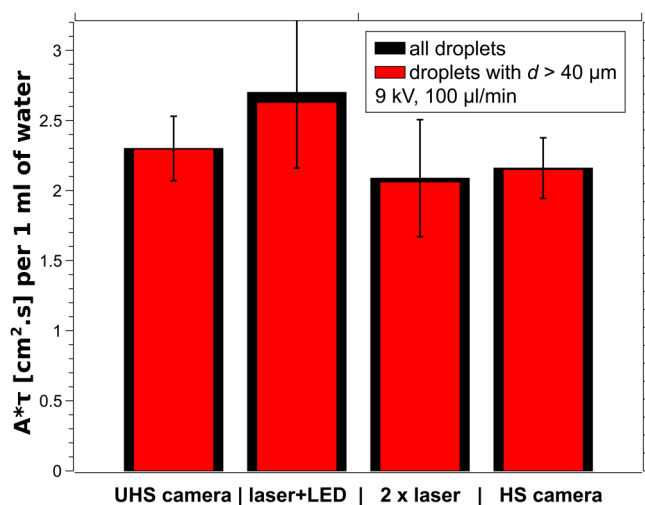


FIG. 16. The solvation capability normalized per unit volume, comparison of $A \times \tau$ values obtained by four different techniques, $V_a = 9 \text{ kV}$, $Q_w = 100 \mu\text{l}/\text{min}$, gap 15.8 mm.

a streamer discharge resulting in bigger droplets' formation. The increase in Q_w shifts the streamer corona onset voltage to higher values and the interference with the ES is less significant, even at 13 kV.

Figure 15 shows ψ_v and ψ_t calculated using data from the UHS camera measurements. Calculation by using the sets of microdroplets detected by laser techniques gives us almost identical results (Fig. 16) and the same trends as from the UHS camera. There is a good agreement within the estimated uncertainty (10%–20%) even if we account for all droplets, not only those with $d > 40 \mu\text{m}$. The reason is that the influence of the smallest microdroplets on ψ_v is marginal. This does not mean that it is not important to create aerosols with fine microdroplets. In fact, it would be great if we could create microdroplets with $d < 50 \mu\text{m}$ only, as they could be nearly saturated by reactive species already during their flying lifetime.⁴³ However, in a real ES influenced by pulsed discharges, microdroplets with a relatively broad size distribution are generated, with the biggest microdroplets playing a significant role. They limit the number of molecules solvated during their lifetime.

IV. CONCLUSIONS

We developed and tested an optical technique for measuring the size of electrosprayed water aerosol microdroplets and determine the droplet size distribution, when studying plasma–liquid interactions and transport of reactive species from the plasma/gas phase into water. Several possible variants of this versatile technique have been tested, with one planar laser, two planar lasers, and one laser combined with incoherent LED light source. The presented technique can reliably recognize droplets with diameter $d > 10 \mu\text{m}$, and the smallest detected microdroplets had an estimated diameter of $d \sim 5 \mu\text{m}$. This is the theoretical detection limit

of our technique for online monitoring of microdroplets. The obtained results were verified by the ultra-high speed camera imaging method. The size distributions of microdroplets with diameter $d > 40 \mu\text{m}$ obtained by the presented optical technique and high-speed camera imaging were almost identical. The differences in size distributions were found only for $d < 40 \mu\text{m}$, which can be explained by a low spatial resolution of camera photographs. However, for a mass transfer of reactive species from plasma into water microdroplets, the smallest microdroplets with $d < 40 \mu\text{m}$ do not play such an important role if the droplets' size distribution is polydisperse, and there is a non-negligible contribution of bigger droplets. The solvation capability of reactive species into water is limited by the biggest microdroplets.

There are several advantages of the presented microdroplet detection technique. It is relatively simple and cost-effective, and it enables a simultaneous online monitoring of the ES and the optical emission spectroscopy or imaging of electrical discharges. The optical signal of the laser close to the nozzle can be even used as a synchronization signal for time-resolved spectroscopy or camera imaging. The electrical signals (discharge currents) can be also recorded and synchronized with the measured optical signals of the microdroplets.

Further modifications and improvements of the presented technique can be easily implemented. For example, a modification planned in near future is to correlate the optical signal attenuation by microdroplets and the decrease in the optical signal (probably at a different wavelength) due to the absorption of plasma species such as O_3 or NO_2 . This microdroplet diagnostic technique will be also used to investigate the influence of the charged vs non-charged microdroplets on the transport of selected plasma species into water, which is still an open fundamental question.

ACKNOWLEDGMENTS

This work was supported by Slovak Research and Development Agency (Nos. APVV-17-0382 and SK-PL-18-0090), Slovak Grant Agency VEGA (No. 1/0419/18), and Comenius University (Grant No. UK/317/2020).

DATA AVAILABILITY

The data that support the findings of this study are available within the article. Additional data that support the findings of this study are available from the corresponding author upon reasonable request.

REFERENCES

- G. Taylor, *Proc. R. Soc. London A* **280**, 383–397 (1964).
- M. Cloupeau and B. Prunet-Foch, *J. Electrostat.* **25**, 165–184 (1990).
- R. P. A. Hartman, D. J. Brunner, D. M. A. Camelot, J. C. M. Marijnissen, and B. Scarlett, *J. Aerosol Sci.* **31**, 65–95 (2000).
- L. Rayleigh, *Philos. Mag.* **14**, 184–186 (1882).
- K. Y. Li, H. Tu, and A. K. Ray, *Langmuir* **21**, 3786–3794 (2005).
- J. Zeleny, *Phys. Rev.* **3**, 69–91 (1914).
- J. Zeleny, *Phys. Rev.* **10**, 1–6 (1917).
- A. K. Ball, S. S. Roy, D. R. Kisku, N. C. Murmu, and C. LdS, *Appl. Soft Comput. J.* **94**, 106438 (2020).

- ⁹S. Kim, M. Jung, S. Choi, J. Lee, J. Lim, and M. Kim, *Exp. Thermal Fluid Sci.* **118**, 110151 (2020).
- ¹⁰Y. Kim, S. Jung, S. Kim, S. T. Choi, M. Kim, and H. Lee, *Int. Commun. Heat Mass Transfer* **118**, 104861 (2020).
- ¹¹J.-P. Borra, *J. Aerosol Sci.* **125**, 208–236 (2018).
- ¹²J. Rosell-Llompert, J. Grifoll, and I. Loscertales, *J. Aerosol Sci.* **125**, 2–31 (2018).
- ¹³A. Jaworek, A. M. Gañán-Calvo, and Z. Machala, *J. Phys. D: Appl. Phys.* **52**, 233001 (2019).
- ¹⁴P. Dwivedi, L. M. Matz, D. A. Atkinson, and H. H. Hill, Jr., *Analyst* **129**, 139–144 (2004).
- ¹⁵A. Jaworek, A. T. Sobczyk, and A. Krupa, *J. Aerosol Sci.* **125**, 57–92 (2018).
- ¹⁶A. Jaworek, *J. Mater. Sci.* **42**, 266–297 (2007).
- ¹⁷H. Cui, N. Li, J. Peng, J. Cheng, N. Zhang, and Z. Wu, *Build. Environ.* **111**, 218–227 (2017).
- ¹⁸C. Carotenuto, F. Di Natale, and A. Lancia, *Chem. Eng. J.* **165**, 35–45 (2010).
- ¹⁹Z. Machala, B. Tarabova, K. Hensel, E. Spetlikova, L. Sikurova, and P. Lukes, *Plasma Proc. Polym.* **10**, 649–659 (2013).
- ²⁰S. K. Boda, X. Li, and J. Xie, *J. Aerosol Sci.* **125**, 164–181 (2018).
- ²¹J. M. López-Herrera, A. Barrero, A. Boucard, I. G. Loscertales, and M. Márquez, *J. Am. Soc. Mass Spectrom.* **15**, 253–259 (2004).
- ²²M. Cloupeau and B. Prunet-Foch, *J. Electrostat.* **22**, 135–159 (1989).
- ²³K. Tang and A. Gomez, *J. Colloid Interface Sci.* **175**, 326–332 (1995).
- ²⁴P. Borra, J. P. Ehouarn, and D. Boulaud, *J. Aerosol Sci.* **35**, 1313–1332 (2004).
- ²⁵N. Puač, M. Gherardi, and M. Shiratani, *Plasma Process. Polym.* **15**, 1700174 (2018).
- ²⁶R. Thirumdas, A. Kothakota, U. Annapure, K. Siliveru, R. Blundell, R. Gatt, and V. P. Valdramidis, *Trends Food Sci. Technol.* **77**, 21–31 (2018).
- ²⁷J. L. Brisset and J. Pawlat, *Plasma Chem. Plasma Process.* **36**, 355–381 (2016).
- ²⁸Z. Machala, B. Tarabová, D. Sersenová, M. Janda, and K. Hensel, *J. Phys. D: Appl. Phys.* **52**, 034002 (2019).
- ²⁹N. K. Kaushik, B. Ghimire, Y. Li *et al.*, *Biol. Chem.* **400**, 39–62 (2018).
- ³⁰J. Kruszelnicki, A. M. Lietz, and M. J. Kushner, *J. Phys. D: Appl. Phys.* **52**, 355207 (2019).
- ³¹G. Oinuma, G. Nayak, Y. Du, and P. J. Bruggeman, *Plasma Sources Sci. Technol.* **29**, 095002 (2020).
- ³²R. Burlica, R. G. Grim, K.-Y. Shih, D. Balkwill, and B. R. Locke, *Plasma Process. Polym.* **7**, 640–649 (2010).
- ³³I. L. Kanev, A. Y. Mikhchev, Y. M. Shlyapnikov, E. A. Shlyapnikova, T. Y. Morozova, and V. N. Morozov, *Anal. Chem.* **86**, 1511–1517 (2014).
- ³⁴Z. Kovalova, M. Leroy, M. J. Kirkpatrick, E. Odic, and Z. Machala, *Bioelectrochemistry* **112**, 91–99 (2016).
- ³⁵H.-H. Kim, J.-H. Kim, and A. Ogata, *J. Aerosol Sci.* **42**, 249–263 (2011).
- ³⁶B. Pongrác, H. H. Kim, M. Janda, V. Martišoviš, and Z. Machala, *J. Phys. D: Appl. Phys.* **47**, 315202 (2014).
- ³⁷A. K. Ball, R. Das, D. Das, S. S. Roy, and N. C. Murmu, *Mater. Today: Proc.* **5**, 7355–7362 (2018).
- ³⁸M. Parhizkar, P. J. T. Reardon, J. C. Knowles, R. J. Browning, E. Stride, R. B. Pedley, T. Grego, and M. Edirisinghe, *Mater. Des.* **126**, 73–84 (2017).
- ³⁹A. Kleitz and J. M. Dorey, *Proc. Inst. Mech. Eng. Part C: J. Mech. Eng. Sci.* **218**, 811–842 (2004).
- ⁴⁰I. Bosdas, M. Mansour, A. I. Kalfas, and R. S. Abhari, *Meas. Sci. Technol.* **27**, 015204 (2016).
- ⁴¹X. Cai, D. Ning, J. Yu *et al.*, *Proc. Inst. Mech. Eng. Part A: J. Power Energy* **228**(2), 153–167 (2014).
- ⁴²L. De Juan and J. Fernández De La Mora, *J. Colloid Interface Sci.* **186**, 280–293 (1997).
- ⁴³M. E. Hassan, M. Janda, and Z. Machala, *Water* **13**, 182 (2021).
- ⁴⁴V. Mitra, A. Sarma, M. S. Janaki, A. N. Sekar Iyengar, B. Sarma, N. Marwan, J. Kurths, P. Kumar Shaw, D. Saha, and S. Ghosh, *Chaos, Solitons Fractals* **69**, 285–293 (2014).
- ⁴⁵P. Ehouarn, L. Unger, and J. P. Borra, *High Temp. Mater. Process.* **5**(3), 333–344 (2001).